

Fatigue crack growth in residual stress fields

garcia, C; Lotz, T; Martinez, MJ; Artemev, A; Alderliesten, RC; Benedictus, R

DOI

[10.1016/j.ijfatigue.2016.02.020](https://doi.org/10.1016/j.ijfatigue.2016.02.020)

Publication date

2016

Document Version

Accepted author manuscript

Published in

International Journal of Fatigue

Citation (APA)

garcia, C., Lotz, T., Martinez, MJ., Artemev, A., Alderliesten, RC., & Benedictus, R. (2016). Fatigue crack growth in residual stress fields. *International Journal of Fatigue*, 87(June), 326-338. <https://doi.org/10.1016/j.ijfatigue.2016.02.020>

Important note

To cite this publication, please use the final published version (if applicable). Please check the document version above.

Copyright

Other than for strictly personal use, it is not permitted to download, forward or distribute the text or part of it, without the consent of the author(s) and/or copyright holder(s), unless the work is under an open content license such as Creative Commons.

Takedown policy

Please contact us and provide details if you believe this document breaches copyrights. We will remove access to the work immediately and investigate your claim.

Fatigue Crack Growth in Residual Stress Fields

Authors: *C. Garcia¹, T. Lotz², M. Martinez^{3,2,1}, A. Artemev¹, R. Alderliesten², R. Benedictus²

Affiliations: ¹ Mechanical and Aerospace Engineering, Carleton University, 1125 Colonel By Drive, Ottawa, ON, Canada K1S 5B6

*Email: christian.garcia@carleton.ca

*Tel.: +52 144 3402 1585

² Faculty of Aerospace Engineering, Delft University of Technology, Kluyverweg 1, P.O. Box 5058, 2600GB Delft, The Netherlands

³ Department of Mechanical and Aeronautical Engineering, Clarkson University, Potsdam, NY, 13699, United States of America

Keywords

7050-T7451; Crack Closure; Plastic Wake; Residual Stress Fields; Finite Element Analysis.

Abstract

A Fatigue Crack Growth (FCG) model for specimens with well-characterized residual stress fields has been studied using experimental analysis and finite element (FE) modeling. The residual stress field was obtained using four point bending tests performed on 7050-T7451 aluminum alloy rectangular specimens and consecutively modeled using the FE method. The experimentally obtained residual stress fields were characterised using a digital image correlation technique and a slitting method, and a good agreement between the experimental residual stress fields and the stress field in the FE model was obtained. The FE FCG models were developed using a linear elastic model, a linear elastic model with crack closure and an elastic-plastic model with crack closure. The crack growth in the FE FCG model was predicted using Paris-Erdogan data obtained from the residual stress free samples, using the Harter T-method for interpolating between different baseline crack growth curves, and using the effective stress intensity factor range and stress ratio. The elastic-plastic model with crack closure effects provides results close to the experimental data for the FCG with positive applied stress ratios reproducing the FCG deceleration in the compressive zone of the residual stress field. However, in the case of a negative stress ratio all models with crack closure effects strongly underestimate the FCG rates,

in which case a linear elastic model provides the best fit with the experimental data. The results demonstrate that the negative part of the stress cycle with a fully closed crack contributes to the driving force for the FCG and thus should be accounted for in the fatigue life estimates.

1. Introduction

Large tensile Residual Stress (RS) fields within engineering components are undesirable because of their negative impact on the components' mechanical properties. If a component has an undetected high level of tensile RS fields then an unforeseen service failure may occur without warning [1-2]. Hence, several thermal and mechanical treatments are routinely used to control the RS fields. For example, on the one hand, the plates of age-hardened aluminum alloys can be uniformly stretched to about 1.5 - 3% strain to relieve the RS fields [3]. On the other hand, the introduction of compressive RS fields on the surface of the components is a common practice used to increase their service life [1-2,4]. Thus, a large number of techniques that can be used to introduce surface layers of compressive RS fields have emerged over the last decades, that is, shot peening, auto-fretting, cold hole expansion, etc.

Structural codes, such as, for example, BS7910 [5], consider the RS fields for the evaluation of components or structures. Additional manufacturing operations such as, for example, post-weld heat treatments, may be used to control the RS levels as recommended by AWS D1.1 [4]. Fastener holes in the aerospace industry are regularly cold worked in order to introduce a surface layer of compressive RS, thus producing the fatigue life increase. However, damage tolerance guidelines for the aeronautical industry should be followed without considering the beneficial effects of cold working treatments that can induce beneficial compressive RS [6]. That is, the effects of RS fields on the service life of engineering components have not yet been completely incorporated into the mechanical design process. For critical components, the control and verification of induced RS fields during manufacturing operations remains a challenge. Moreover, the pre-existing RS fields may evolve during the service life of the components, thus adding complexity to the consideration of the effects of RS fields on the design of mechanical components. From the damage tolerance perspective, it is necessary to develop reliable models for an accurate prediction of the Fatigue Crack Growth (FCG) in RS fields so that unforeseen service failures may be prevented and the actual service life may be extended.

Different versions of the elastic superposition method have been used to analyze FCG in RS fields [7, 8, 9, 10, 11] since the introduction of the damage tolerant design. The main differences in publications on the analysis of FCG in RS fields are the usage of either a total stress intensity factor range or an effective stress intensity factor range. The stress intensity

factors due to external loads and due to pre-existing RS fields in the uncracked component are added together in the total stress intensity factor approach, which can either include or exclude crack closure effects. In the case of the effective stress intensity factor range approach (ΔK_{eff}), the applied cyclic load that first overcomes the crack closure effect in the component is determined and used to calculate a crack opening stress intensity factor (K_{op}). The K_{op} is subtracted from the nominal K_{max} to define the effective stress intensity factor range. Beghini et al. [7-8] conducted experimental FCG tests in RS fields at the constant amplitude stress and stress ratio $R = 0.1$, and used the linear elastic superposition-based method to analyze the experiments. The studies were conducted using welded Compact Tension (CT) specimens, which were made of a C-Mn microalloyed steel joined by the gas metal arc welding (GMAW) process [7] and API 5L X65 steel joined by laser welding process [8]. For all the CT specimens, the RS fields were determined by the slitting method. The results indicated that the superposition-based method could give adequate results if the RS field gave a positive contribution to the stress intensity factor, i.e., for tensile RS fields, but it was not the case for the compressive RS fields [7-8]. Such difference was attributed to the lack of the crack closure effect [12] associated with the crack tip plasticity [8].

Other publications based on linear elastic superposition by Jones and Dunn [9-10] used the Finite Element (FE) method to compute the total stress intensity factors and to model the FCG in RS fields. The pre-existing RS fields in the un-cracked specimens were used as crack face pressures in the analysis and in the FE models in order to compute the total stress intensity factor, and the redistribution of the RS field was not considered. The model results were compared with experimental data obtained on the Single-Edge Bend (SE(B)) specimens fabricated with the 2024-T351 aluminum alloy [9], and the cold-hole expanded specimens fabricated with the 7075-T651 aluminum alloy [10]. In the case of the SE(B) specimen, the experimental FCG tests with the constant stress intensity factor range and $R = 0.1$ were conducted to verify the analysis, while the FCG tests with a constant applied stress amplitude and $R = 0.1$ were employed for the cold-hole expanded specimen. The results obtained for the SE(B) specimens indicated that the computational model was able to predict the experimental FCG rates within the factor of 2, provided that the crack closure effect was considered [9]. For the cold-hole expanded specimen, the results demonstrated a poor correlation between the model and the experiments [10]. The principal reason for the poor performance of superposition-based

FE model was attributed to inaccuracies in the pre-existing RS field determination and lack of consideration of the redistribution of RS field due to FCG [10].

During the FCG process, forward and backward plasticity zones are developed at the crack tip and a plastic wake is left on the path of the growing crack. A direct consequence of these effects is the crack closure effect discovered by Elber [12]. At the current state-of-the-art, the effective stress intensity factor range method focuses on determining the fraction of the applied stress range, or the crack opening stress, that overcomes the crack closure effect. For this purpose, experimental, empirical relations and plasticity-induced crack closure analyses with the FE method have been developed to determine the crack opening stress. Solanki et al. [13] provided an overview of the plasticity-induced fatigue crack closure analysis with the FE method. LaRue and Daniewicz [11] developed a model predicting the FCG through a RS field based on the effective stress intensity factor range method. Furthermore, they conducted an analysis based on the linear-elastic superposition method. A 2D elastic-plastic FE model was employed to compute the crack opening stress. The computational model results were compared to the experimental data published in [14]. The results indicated that the effective stress intensity factor method provided better estimates of the FCG in RS fields than the superposition-based method when compared with the experimental data [11]. There is an intense debate in the literature between the supporters of the elastic superposition method [15-16] and those who question its applicability for the prediction of the FCG in RSF [17, 18, 19]. For the components manufactured with surface layers of compressive RS fields, the elastic superposition method has failed to provide reliable FCG predictions [20, 21, 22, 23, 24]. The published studies of the FCG in RS fields and the FCG models used in them do not provide quantitative information on a possible effect of plasticity wake on the FCG. The plasticity wake can result in the crack closure and reduction of the effective stress intensity range. This effect can be especially significant in the case of the FCG with negative stress ratios, however, most studies of the FCG in RS fields were performed for positive stress ratios.

This paper reports on the experimental and computational FCG study of large cracks propagating in an RS field in single edge notched tension (SENT) specimens made of 7050-T7451 aluminum alloy. Different models of crack propagation were studied in FE simulations, which were performed for the FCG with nominal stress ratios $R = 0.05$ and -1.0 . The FE simulations provide the results for the effective K , which was defined as the stress intensity

factor associated with the combined external and internal loads. The internal loads were associated with redistributed RS fields due to the FCG, and possible crack closure or plastic wake effects. As such, the effective ΔK is considered to be the effective K_{max} minus the effective K_{min} , evaluated at both the maximum and minimum cyclic loads.

2. Material characterization

Any possible RS field in the as-received condition of the 7050-T7451 aluminum alloy plate was regarded as negligible according to the specified temper designation [3]. Single edge notched tension (SENT) specimens used for the FCG tests were manufactured by milling operations. The notch was cut perpendicular to the rolling direction. The dimensions of the SENT specimens were: 254.0 mm length by 50.8 mm width by 12.7 mm thickness. Low speed and depth cuts were applied to minimize machining-induced RS fields [25]. An as-machined dog-bone specimen was used to determine the mechanical properties of the 7050-T7451 aluminum alloy under a uniaxial tension test. The elastic modulus E was 70.2 GPa; the yield strength $\sigma_{0.2\%}$ was measured to be 466 MPa; the ultimate strength σ_u was measured at 523 MPa while the ultimate strain ϵ_u was 0.082. The mechanical properties were in agreement with standard specifications for this alloy found in the literature [3].

A servo-hydraulic machine with a load cell of 100 kN was used for all the FCG tests conducted in this study. A starting notch with the depth of 0.5 mm was machined into the SENT specimens by electro-discharge machining (EDM) with a 0.1 mm wire. The SENT specimens were clamped by hydraulic grips into the servo-hydraulic fatigue machine. Baseline FCG tests were performed on SENT specimens in the as-machined condition (without pre-existing RS fields). FCG tests were also conducted on SENT specimens with a pre-existing RS field introduced by a four-point-bending test, as explained in the following section. A sinusoidal constant load ratio with the frequency of 25 Hz was applied for the crack initiation and the subsequent FCG test. Only at the end of the FCG test (unstable FCG regimen), the frequency was reduced to 5 Hz to allow a proper measurement of the crack length. Pre-cracking was conducted until the initial crack length of 1.5 mm. The FCG tests were conducted under constant stress amplitudes (increasing ΔK) at the stress ratios and maximum applied stresses of $R = -1$ and $\sigma_{max} = 54.25$ MPa; $R = 0.05$ and $\sigma_{max} = 54.25$ MPa; and $R = 0.7$ and $\sigma_{max} = 85.25$ MPa. The stress ratio and the maximum applied stresses for pre-cracking were the same as for the

corresponding FCG test. The crack length at the front- and back-sides of the specimen was monitored with two digital cameras during the crack propagation. Figure 1 presents the baseline fatigue crack growth (FCG) data of the 7050-T7451 aluminum alloy. The fatigue crack growth rate was computed with a polynomial regression method as described in the ASTM E647 standard [26]. A weight function developed by Ahmad *et al.* [27] was used to compute the stress intensity factor for the SENT specimens with clamped ends.

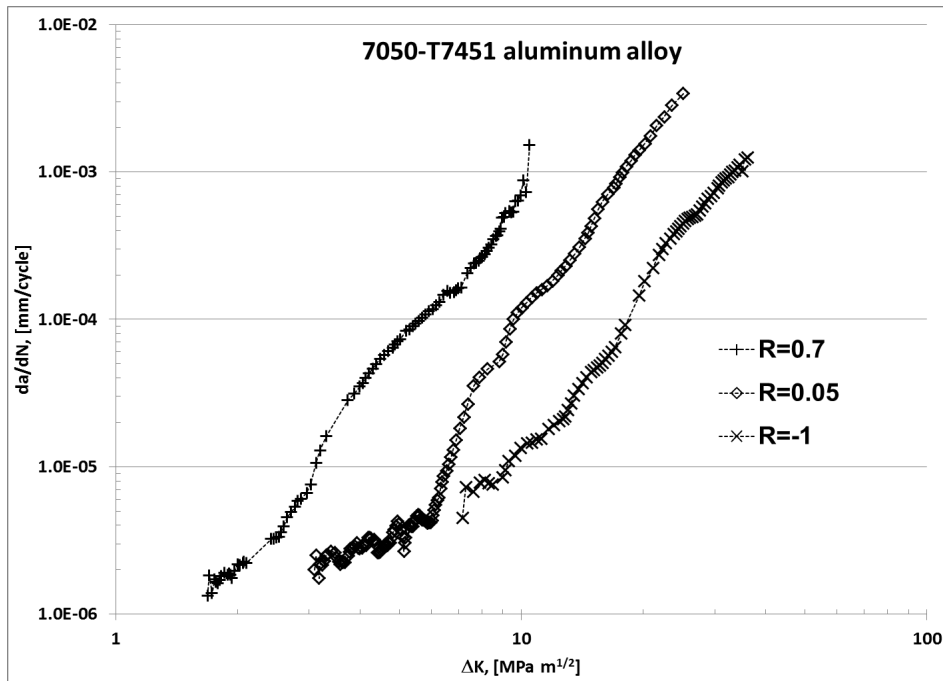


Figure 1. 7050-T7451 aluminum alloy baseline fatigue crack growth rate (FCGR) data.

According to the Irwin model, the upper bound for the plastic zone radius developed in the experimental baseline FCG tests was of 0.122 mm (plane stress condition). This value was determined for the SENT specimen tested at $R=0.7$, $\Delta K = 10.47 \text{ MPa}\cdot\text{m}^{1/2}$ and the critical crack length of 23.6 mm, thus producing the largest plastic zone. The minimum planar dimension, that is, the thickness of the specimen, 12.7mm, was at least two orders of magnitude larger than the largest plastic zone in the SENT specimens. This relationship resulted in a predominantly linear-elastic behavior. The FCG data for the 7050-T7451 aluminum alloy specimens (Figure 1) was therefore within the small scale-yielding criterion.

3. FCG in RS fields experiments

FCG tests were conducted on the SENT specimens with a RS field previously introduced by a non-uniform plastic deformation process. Rectangular bars of the 7050-T7451 aluminum alloy were bent at a displacement rate of $\sim 9 \mu\text{m s}^{-1}$ on a manually operated machine with a four-point-bending test configuration (fig. 2a). A strain gauge was placed on the upper and lower faces of the beam specimen. The four-point-bending test was designed to introduce a strain of $10,000 \mu\epsilon$ at the outer surface of the beam specimen, at an equivalent load of $\sim 90\text{kN}$. The applied load was monitored in real time and the strain was measured at each applied load increment ($\Delta P = 2 \text{ kN}$) so that the four-point-bending test was conducted until it reached the strain value just above $10,000 \mu\epsilon$ on the lower strain gauge (fig. 2a). Digital Image Correlation (DIC) [28] and slitting [29] tests were employed to determine the residual strain profile and the RS fields introduced by the four-point-bending test and to verify the FE results. The sample zone for the beam specimens in the DIC technique was focused at the center of the specimens as shown in Figure 2a, while the slitting method was conducted over the mid-section of the specimen's length, i.e., the position of the notch, which corresponded to the expected crack growth plane. The DIC technique was used during the four-point bending treatment of all the beam specimens analyzed in this research, and the slitting method was used only for two beam specimens as a destructive technique to verify the procedure utilized to introduce the residual stress field.

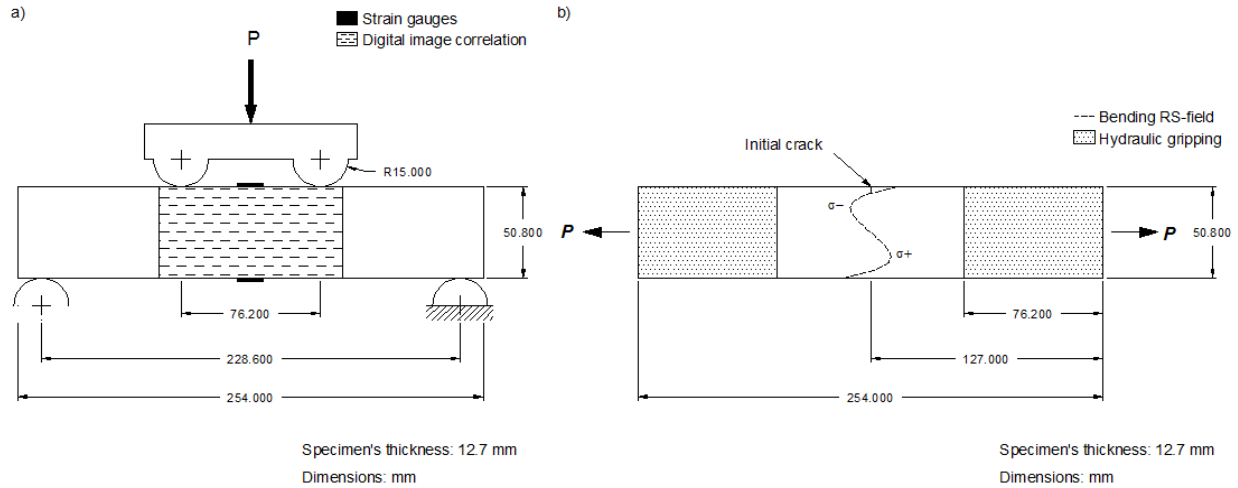


Figure 2. a) Design of the four-point-bending test and b) SENT specimen for the fatigue crack growth (FCG) test with a schematic plot of the residual stress field introduced by four-point-bending (initial notch placed at tension side of RS-field).

Once the four-point-bending procedures were accomplished, the strain gauges on the beam specimens were removed and a notch was machined by EDM into the side of the beam specimen containing the tensile RS stress. As a result, the beam specimens were modified into SENT specimens with a redistributed RS field (Fig. 2b). The EDM notch and FCG test procedures were identical to those described in the previous section. In total, two FCG tests were conducted for the SENT specimens with a redistributed RS field. The FCG test conditions were $R = 0.05$ and $\sigma_{max} = 54.25$ MPa for the first specimen, and $R = -1$ and $\sigma_{max} = 54.25$ MPa for the second specimen.

3.1 Fatigue crack growth model

An effective stress intensity factor approach was used to analyze the effect of the RS fields on the FCG. The predictions of the FCG rate were based on the following correlation:

$$\frac{da}{dN} = f(\Delta K, R) \dots \dots \dots (1)$$

where $\Delta K = K_{max} - K_{min}$, $R = K_{min}/K_{max}$ and $da/dN =$ crack growth per cycle. The fatigue life was predicted by:

$$N = \int_{a_0}^{a_1} \frac{da}{f(\Delta K, R)} \dots \dots \dots (2)$$

Although the experimental FCG tests were conducted under a constant amplitude load (fixed stress ratios of $R = 0.05$ and -1), the RS field produced by the four-point bending operation on the specimens induced variable stress ratios R at the local domain of the crack tip during the FCG tests. Therefore, the baseline FCG curves at $R = 0.05$ and -1 (fig. 1) and a single relationship as expressed in equation (1), e.g., Paris-Erdogan relationship, were not adequate to predict the FCG rates. Instead, variable stress ratios R produced by the RS field in the FCG rate were considered in the model by using the numerical interpolation Harter T-method [30] that can be used to determine new FCG data ($\Delta K_i, R_{int}$) for the stress ratio of interest R_{int} . The interpolation technique is based on the relationship that is obtained by combining the Walker and Paris-Erdogan relationships:

$$\frac{da}{dN} = C \left[\frac{\Delta K}{(1-R)^{(1-m)}} \right]^n \dots \dots \dots (3)$$

where C , m and n are all empirical parameters. Harter T-method linearly interpolates the m assuming that the FCG curves at that particular da/dN are parallel. Knowing two FCG data points ($R_2 > R_1$) at a constant crack growth rate (fig. 3a), the exponent m is obtained according to the following relationships [30]:

$$\begin{aligned}
 m &= 1 + \left[\frac{\log_{10} \left(\frac{\Delta K_1}{\Delta K_2} \right)}{\log_{10} \left(\frac{1-R_2}{1-R_1} \right)} \right] && \text{for } R_1 \text{ and } R_2 \geq 0 \\
 m &= 1 + \left[\frac{\log_{10} \left(\frac{K_{max1}}{\Delta K_2} \right)}{\log_{10} \left((1-R_1)(1-R_2) \right)} \right] && \text{for } R_1 < 0 \text{ and } R_2 \geq 0 \dots \dots \dots (4) \\
 m &= 1 - \left[\frac{\log_{10} \left(\frac{K_{max1}}{K_{max2}} \right)}{\log_{10} \left(\frac{1-R_2}{1-R_1} \right)} \right] && \text{for } R_1 \text{ and } R_2 \leq 0
 \end{aligned}$$

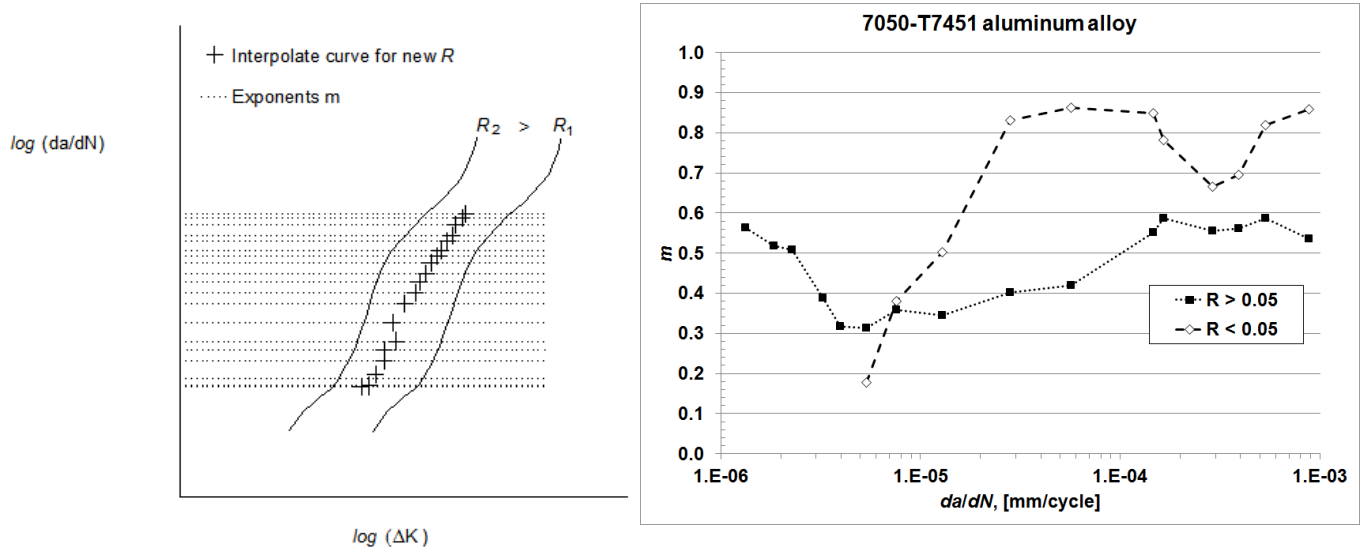


Figure 3. a) Representation of the interpolation process (Harter T-method [30]) to compute FCG curves for any arbitrary stress ratio of interest. Solid lines represent baseline curves and crosses represent the result of interpolation. b) Calculated values of the m -exponent for the Harter T-method.

In the present work, several exponents m_i were determined within the range of the FCG rates from approximately 5.0×10^{-6} to 1.0×10^{-3} mm/cycle. This range covered all crack growth rates obtained in the FCG model. Sixteen exponents m_i were used for $R_{int} > 0.05$ and eleven exponents m_i were used for $R_{int} < 0.05$ (fig. 3 b). The analysis was limited to large cracks and stable crack growth regime. The crack nucleation and short crack behaviour were out of the scope of this research. The baseline FCG data at $R = 0.05$ ($\Delta K_1, R_1$) of the 7050-T7451 aluminum alloy (fig. 1) and the computed variable m_i were employed to find a new FCG data at R_{int} :

$$\Delta K_i = \Delta K_1 \left(\frac{1-R_1}{1-R_{int}} \right)^{m_i-1} \quad \text{for } R_{int} \geq 0$$

..... (5)

$$\Delta K_{max_i} = \Delta K_1 \frac{(1-R_1)^{m_i-1}}{(1-R_{int})^{1-m_i}} \quad \text{for } R_{int} < 0$$

Each obtained value of ΔK_i corresponds the definite value of crack growth rate $(da/dN)_i$, and the set of ΔK_i and $(da/dN)_i$ values determines $da/dN(\Delta K, R_{int})$ relationship.

3.2 Finite element model

The commercial package ABAQUS [31] was employed to create a finite element (FE) model, which was used to simulate four-point-bending of a beam specimen and a FCG in specimens with RS field. To simulate the FCG in the RS field, the beam specimen with the initial RS field induced by four-point-bending was modified into a SENT specimen. This modification occurred by introducing a starter crack with the length of 5.08 mm on the tension RS side of the specimen along its symmetry plane. Figures 4 a, b present the FE model, which consisted of the beam specimen, lower/upper roller parts (four-point-bending test), and contact surface/grip parts (FCG test). To reduce the modeling complexity and the required computing resources, only half of the specimen was modeled by employing the y - z plane of symmetry (shown in fig. 4a). Eight-node linear brick elements with a reduced integration scheme (C3D8R) were used in the FE model. Figures 4 c, d show the refined mesh used in the crack tip region in the FE model. The refined mesh region has dimensions 2.032×2.032 mm, with an element size of 127 μm or 56 μm .

In the case of the four-point-bending simulation, the contact interaction imposed between the beam and the lower/upper rollers was essential to properly capture the non-linear load distribution and the boundary conditions present in the experimental setup. Preliminary FE models developed in this study, which made use of concentrated loading rather than contact loading, were able to successfully capture the RS field from a qualitative perspective. However, the residual strain and stress fields obtained with FE models using a contact loading condition produced results that more closely approximated those from the slitting and digital image correlation techniques. In the case of the FCG simulation, the contact loading set for the clamping was essential for the reproduction of the non-uniform stress distribution at the grip region of the SENT specimen. Moreover, the contact loading at the grip with no external applied load caused a redistribution of the RS field around the crack tip that completely modified the crack propagation during the simulated fatigue test. Thus, for this study it was essential to take into account the grip contribution during the FCG simulation.

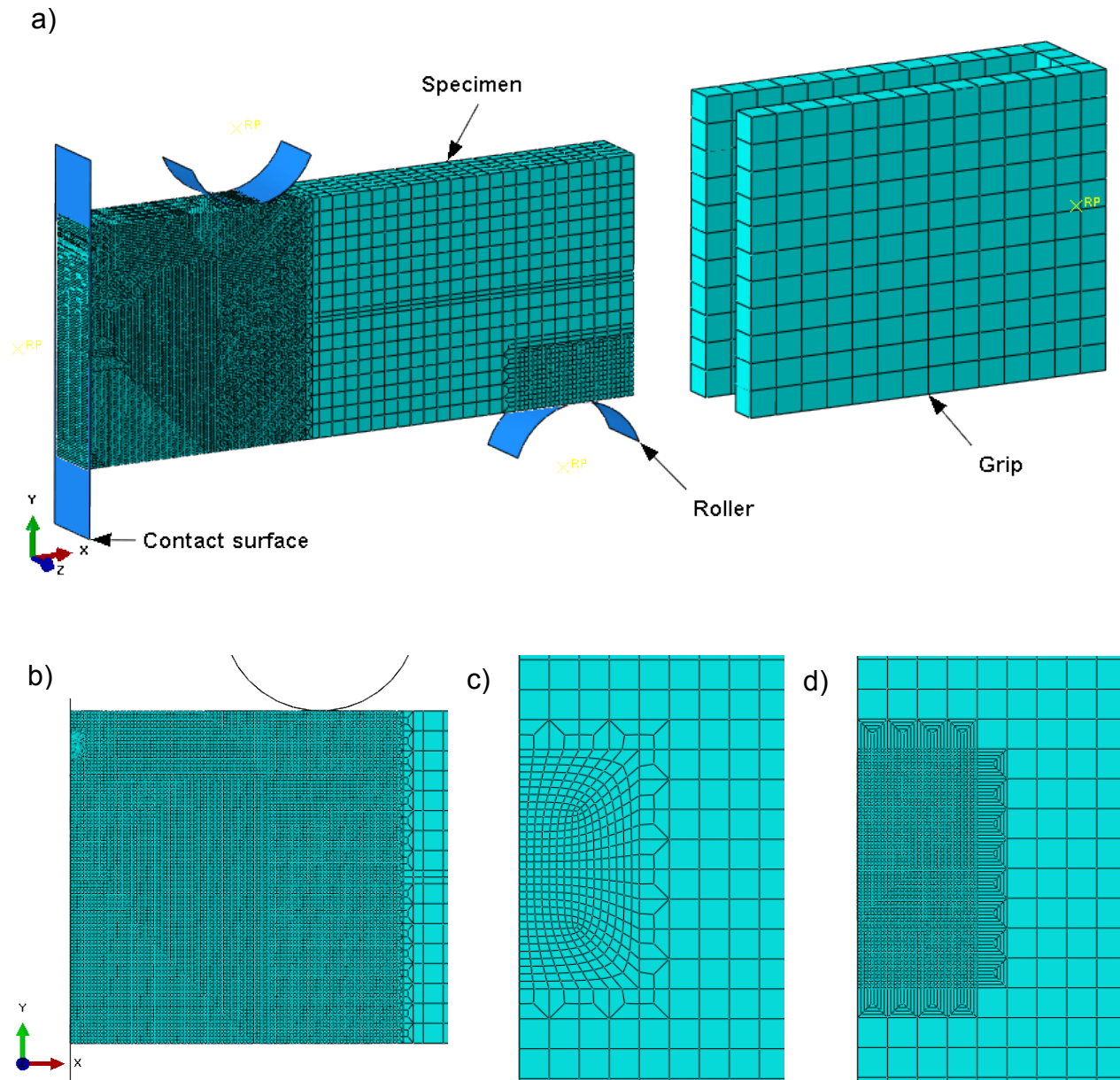


Figure 4. Half-symmetry finite element (FE) model: a) Beam specimen, rollers, grip, and contact surface parts, and b) mesh detail of the specimen with the initial crack length of 5.08 mm. c) Focused mesh at crack tip region, and d) refined mesh at crack tip region to model the plastic wake effect.

The effective stress intensity factors K_{max} and K_{min} were computed from the FE results with a displacement correlation method [32]. Such stress intensity values include contributions from the external load and RS field. The effective stress intensity factors were computed along the crack face at different distances from the crack tip [32], according to the plane strain condition:

$$K_I = \frac{Eu}{4(1-\nu^2)} \sqrt{\frac{2\pi}{r}} \dots\dots\dots (6)$$

where E is the elastic modulus, ν is the Poisson's ratio, r is the distance from the crack tip to the node position (fig. 5 a) and u is the displacement at the node position in the direction aligned with the cyclic load. Equation (6) is formulated for a plane strain condition, which is satisfied during the stable FCG because of the thickness of the SENT specimen. The distribution of the effective K_I values obtained for the crack with the length of 6.096 mm under a maximum applied load in the cycle with $R = 0.05$ is shown in fig. 5 b. The K_I values have strong fluctuations near the crack tip, however, they demonstrate the asymptotic linear behaviour at larger distances from the crack tip. According to the displacement correlation method [32], only a well defined linear part of the K_I distribution was used to define the effective K_I value at the crack tip by extrapolating this linear relationship to $r = 0$. This approach was used to calculate the effective stress intensity factors K_{max} and K_{min} at the maximum and minimum loads. It is important to note that RS field changes resulting from the crack growth were taken into account in this model while the distribution of the plastic deformation produced during four-point-bending remained unchanged. In contrast, the superposition models used in [7, 8, 9, 10] the RS field remained unchanged during the FCG.

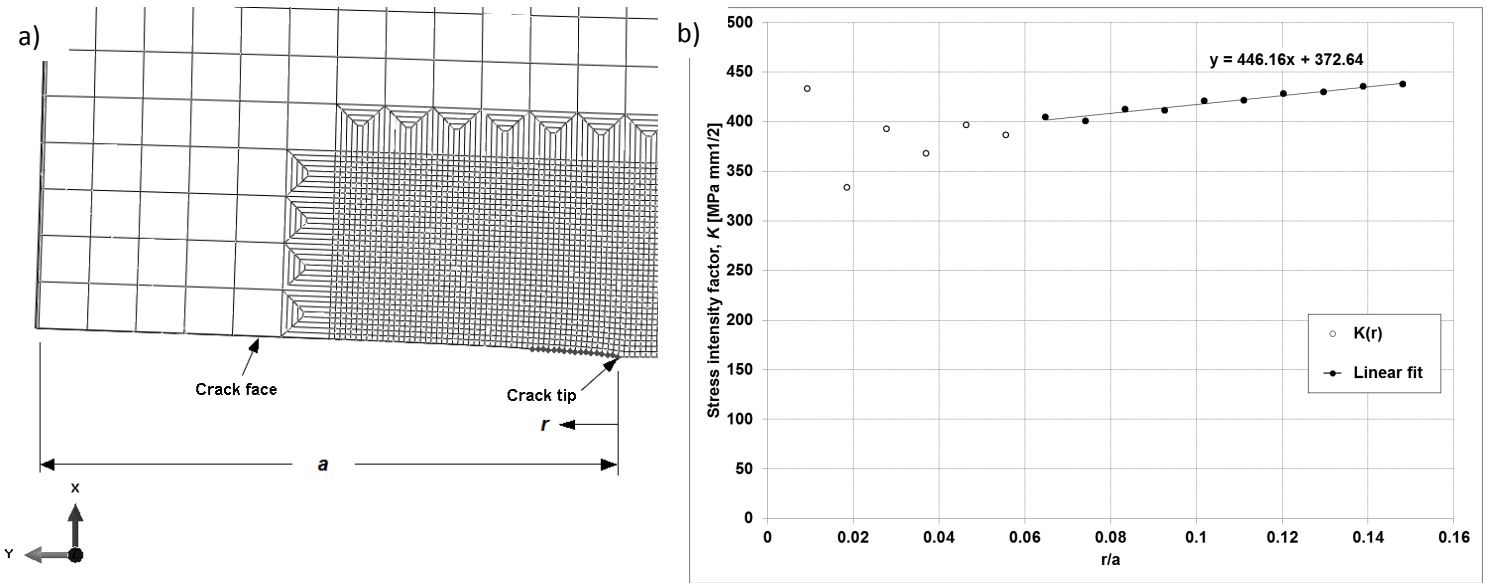


Figure 5. Determination of maximum stress intensity factor K_{max} for a 6.096 mm crack length with the displacement correlation method. a) Nodes selected behind the crack tip. b) Linear fit of the effective K and extrapolation back to the crack tip.

The RS field distributions obtained in the FE model with different crack lengths at the zero applied load conditions are shown in fig. 6. For the crack lengths equal to 5.08, 7.62 and 10.16 mm, the RS field is completely relaxed (zero stress state) on the crack surface for the nodes behind the crack tip, while for the nodes in front of the crack tip, the RS field is redistributed as compared to the initial RS field. At these crack lengths the RS redistribution results in the change from the compression stresses in the initial RS field to the tension stresses in the redistributed RS fields at the crack tip. In the case of the crack lengths equal to 12.7, 17.78 and 22.86 mm, the RS field was redistributed without changing the stress state from compression to tension (the corresponding stress distributions within the refined mesh regions are shown in fig. 6) and the crack was partially closed with several nodes on the crack surface behind the crack tip remaining in full contact with the opposite surface of the crack.

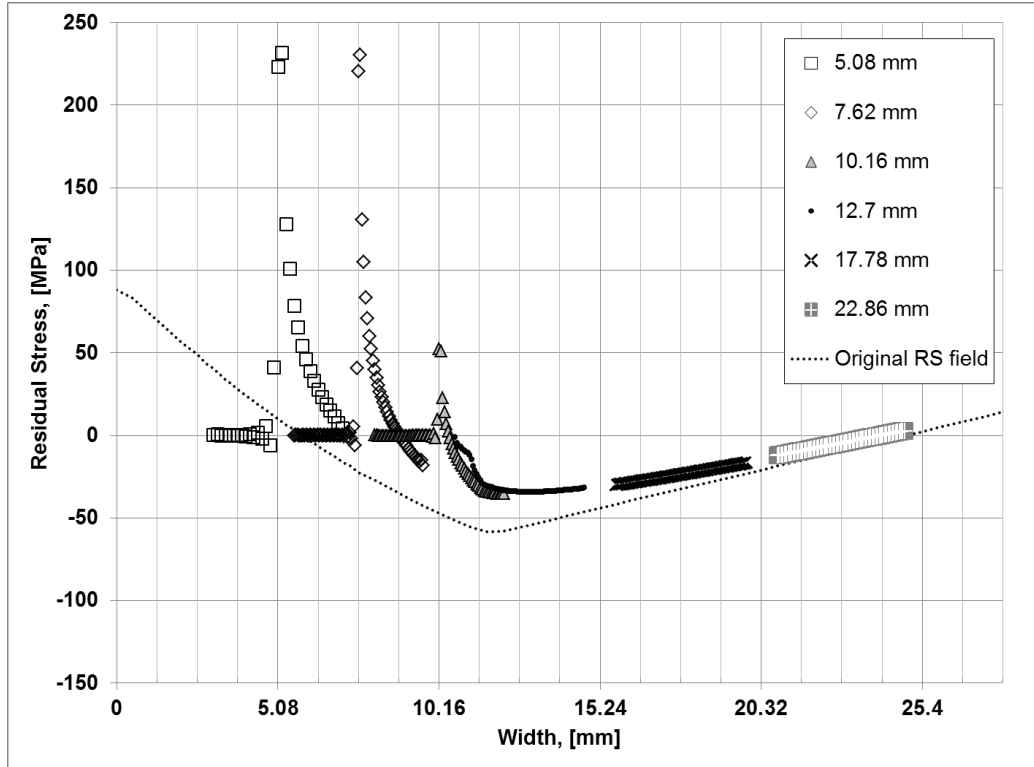


Figure 6. The relaxation and redistribution of the RS field due to the FCG at zero applied load.

3.3 Four-point-bending test simulation

The rollers (Fig. 4 a) were modeled as rigid bodies and had a load of 90 kN applied to them. The four-point-bending test simulation was accomplished in four steps: the initial step set by default in ABAQUS to set up possible initial conditions; the second step to initiate the contact interactions between the rollers and the specimen; the third step to apply the load to the upper roller and the final step to release the load, after which the misfit plastic strains of the inhomogeneous bending deformation resulted in a well-known RS field in the beam specimen. The mechanical properties of the 7050-T7451 aluminum alloy determined from the uniaxial tension test were employed to define the elastic-plastic material behavior in the FE model. The elasticity was simulated with the Young's modulus E of 70 GPa and the Poisson's ratio of 0.33, while plasticity was simulated with a von Mises yield function, associate flow rule and combined hardening model defined by a series of true stress and true plastic strain coordinate pairs $(\sigma_n, \varepsilon_n^p)$. As will be presented in the results and discussion section, the standard initial yield point σ_0 at the 0.2% proof stress (466 MPa) resulted in the overestimation of the RS field introduced

by the four-point-bending test as shown by the slitting results. Previous studies of the subject had proved that a proper characterization of the pre-existing RS fields was crucial to analyze the behavior of the FCG in RS fields [9-10, 33]. Thereby, the standard initial yield point σ_0 at the 0.2% proof stress was not employed; rather it was calculated using the 0.025% proof stress, resulting in a true stress value of 397 MPa. Successive yield points σ_n ($n = 1, 2 \dots 5$) for the combined hardening model (kinematic and isotropic) were calculated using the 0.05, 0.075, 0.1, 0.2 and 4 % proof stresses, resulting in the true stress values of 435, 450, 458, 466 and 538 MPa. The associated true plastic strains ε_n^p were equal to 0, 0.000502, 0.000752, 0.001001, 0.001879 and 0.042317, respectively. This definition of the combined hardening model was also employed for the FCG test simulations.

3.4 Fatigue crack growth simulation

A through-thickness starter crack was introduced into the beam specimen, containing an initial RS field produced by the simulation of four-point-bending, on the specimen side with a tension RS field. After the introduction of the starter crack, the grip (fig. 4 a) was applied to the specimen for the FCG test (fig. 2 b). The grip was meshed with eight-node linear brick elements, but it was defined as a rigid body with a reference point to apply maximum and minimum cycle loads (P_{max} and P_{min}). The contact conditions between the grip and the specimen were formulated with a penalty method [31] and the “rough” friction option was used to prevent any possible slipping between the surfaces. Only an elastic slip associated with the penalty method is allowed by the “rough” friction formulation [31].

The FCG test was simulated by applying P_{max} and P_{min} cycle loads to the SENT specimen for several crack lengths a_n . A total of 41 crack lengths were modeled (constant crack increment $\Delta a = 0.508$ mm) from the initial crack length $a_0 = 5.08$ mm to the final crack length $a_{40} = 25.4$ mm. The region around the crack tip was re-meshed for each crack length. Figure 4b shows the mesh of the SENT specimen for the initial crack length $a_0 = 5.08$ mm placed on the upper side of the specimen (tension RS field). The effective K_{max} and K_{min} values were computed according to one of the three FE FCG models described below. The effective ΔK and R corresponding to the obtained K_{max} and K_{min} values were used in the Harter T-method based numerical procedure to calculate the number of the load cycles required for crack to propagate to a new crack length. After which the crack length was increased with a refined mesh to a new crack tip position.

3.4.1 Linear elastic model without rigid crack closure conditions (LE Model)

In the LE Model only the linear elastic deformation was considered and there was no limit imposed on the crack surface displacements preventing it from the overlapping with the second half of the SENT specimen, which was removed from the FE element model using the symmetry of the specimen. As a result, this model can produce negative K_I values appearing as a result of negative applied stresses and/or negative RS near the crack tip. As compared to the two other models presented in this study, this model produces the largest ΔK values under such conditions.

3.4.2 Linear elastic model with rigid crack closure conditions (LE RCC model)

To prevent negative values of the effective K_{min} , the crack closure effect was incorporated into the linear elastic FE model by introducing a rigid surface with a reference point on the symmetry plane of the specimen (fig. 4a). Boundary conditions were applied to the rigid surface on the reference point to prevent any possible displacement and translation (encastre condition) during the FCG simulation. The contact normal conditions between the rigid surface and the crack face on the SENT specimen were defined with an augmented Lagrange formulation. The contact interaction prevented negative values of displacements and K_I .

3.4.3 Elastic-plastic model with rigid crack closure conditions (EP RCC Model).

A plasticity-induced crack closure FE analysis was conducted by using the elastic-plastic material model in FE calculations. This model described the plastic zone at the crack tip and plastic wake formed along the crack surface. The basic approach to the FE analysis remains similar; a cycle loading is applied for each crack length a_n , but the crack is advanced one element size by releasing the nodes at the crack tip. The process is repeated several times to allow a plastic wake formation. The refined mesh around the crack tip with the smallest element size of 0.056 mm was used in this model to resolve the plastic zone and plastic wake. According to the Irwin plastic zone equation, the radius of the plastic zone r_p at the crack tip can be defined as:

$$2r_p = \frac{1}{\alpha\pi} \left(\frac{K_{max}}{\sigma_{YS}} \right)^2 \dots\dots\dots (7)$$

where α is 1 and 3 for either plane stress or plane strain and σ_{YS} is the yield stress. According to a plane stress state of the front and back surfaces of the SENT specimen and with the P_{max} cycle load, the initial crack length (5.08 mm) showed the r_p of 0.068 mm (68 μm). Therefore, the element size employed in the previous FE analyses (127 μm) was not able to resolve the plastic zone at the crack tip. Thus, the focused mesh at the crack tip was refined to the element size of 0.056 mm (56 μm) to guarantee at least two elements in the plastic zone at the crack tip. However, the number of elements present in the plastic zone during the FCG simulation was also a function of the redistributed RS field. As a result, the total number of elements with a plastic condition for the initial crack length of 5.08 mm was fifteen, which was a large number because of the positive distribution of the RS field present around the crack tip. The fifteen elements with a plastic condition at the initial crack length evolved during the FCG simulation, and reached a minimum of five elements for a crack length of 10.16 mm and a maximum of twenty-eight for the crack length of 25.4 mm. The number of elements under the plastic condition drops while the propagated crack tip crosses a negative residual stress distribution region despite an increase of the crack length.

4. Results and discussion

4.1 Residual strain and stress fields

The residual stress and strain fields that were introduced by the four-point-bending test into the beam specimens are shown in figure 7a and 7b. A good correlation between the FE and experimental results were observed using a material model with the yield stress corresponding to 0.025% offset. The results were plotted for the middle length of the specimen, i.e., the plane of the crack growth for the specimens (symmetry plane). In the case of the RS field (fig. 7a), the stress distribution was a zigzag pattern as a function of the width of the specimen, defined by four peak points (tension, compression, tension and compression sign) and three neutral points (zero stress axes). The differences between the numerical (FE) and experimental (slitting) results were ~ 5 , ~ 10 and ~ 40 MPa for the tension, compression-tension and compression peak points respectively. In the case of the residual strain field (fig. 7b), the strain distribution was linear as a

function of the width of the specimen, defined by one neutral point (zero strain axis). The difference between the FE and DIC results was $-250 \mu\epsilon$ and $350 \mu\epsilon$, respectively, for the initial

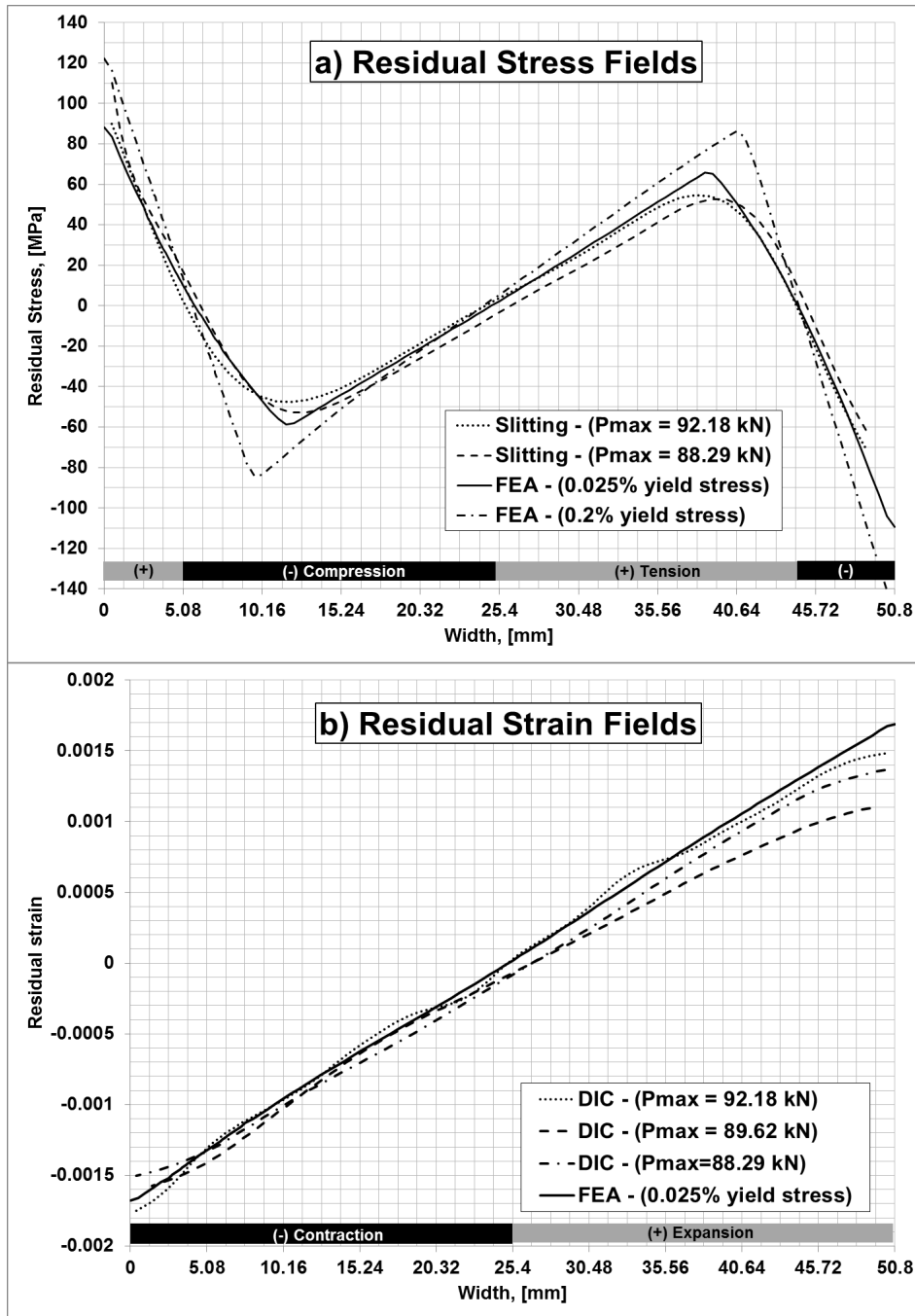


Figure 7. The numerical (FE) and experimental (Slitting and DIC) results at the mid position (symmetry plane) of 7050-T7451 aluminum alloy specimens after the four-point-bending test: a) residual stress fields, and b) residual strain fields.

and the final sections of the specimen's width. Neither the DIC nor the slitting methods were capable of resolving the stress and strain distribution at the edges of the specimen because of natural limitations of the techniques [28-29]. For instance, the peak point of compressive RS was not at the final section of the specimen's width, but instead 2 mm before the final section where the difference between the FE and slitting results was less than 10 MPa. The numerical and experimental results indicated that a well-known, consistent and repeatable RS field was introduced into the beam specimens. For RS fields that are constant through the specimen's thickness, the slitting method is considered the most reliable measurement technique [34]. Finally, figure 7a also shows the FE results that correspond to the same 7050-T7451 aluminum alloys and the FE model (fig. 4a), but with an initial yield point defined by the standard 0.2% proof stress. As observed, the standard yield stress at 0.2% proof stress resulted in the overestimation of the RS field produced by the FE model.

4.2 Fatigue crack growth model and experiments

4.2.1 $R = 0.05$

Fig. 8 presents the effective ΔK and R obtained using the three FCG models: the Linear Elastic (LE), the Linear Elastic with Rigid Crack Closure conditions (LE RCC), and the Elastic-Plastic with Rigid Crack Closure conditions (EP RCC). In addition, horizontal bars indicate the types of stress states in the original RS field distribution produced by four-point-bending. $\Delta K(a)$ relationships, which were significantly different, were obtained using a model that included the rigid crack closure conditions and a model that excluded them. In the model without rigid crack closure conditions, ΔK increases with the increase in a continuously, while both models including rigid crack closure conditions produced $\Delta K(a)$ curves reaching maximum at 10-11 mm, then decreasing to the minimum at 12-13 mm and then increasing until the final failure event. The location of the first maximum differed from the location at which the original RS field produced by four-point-bending changed from tensile to compressive.

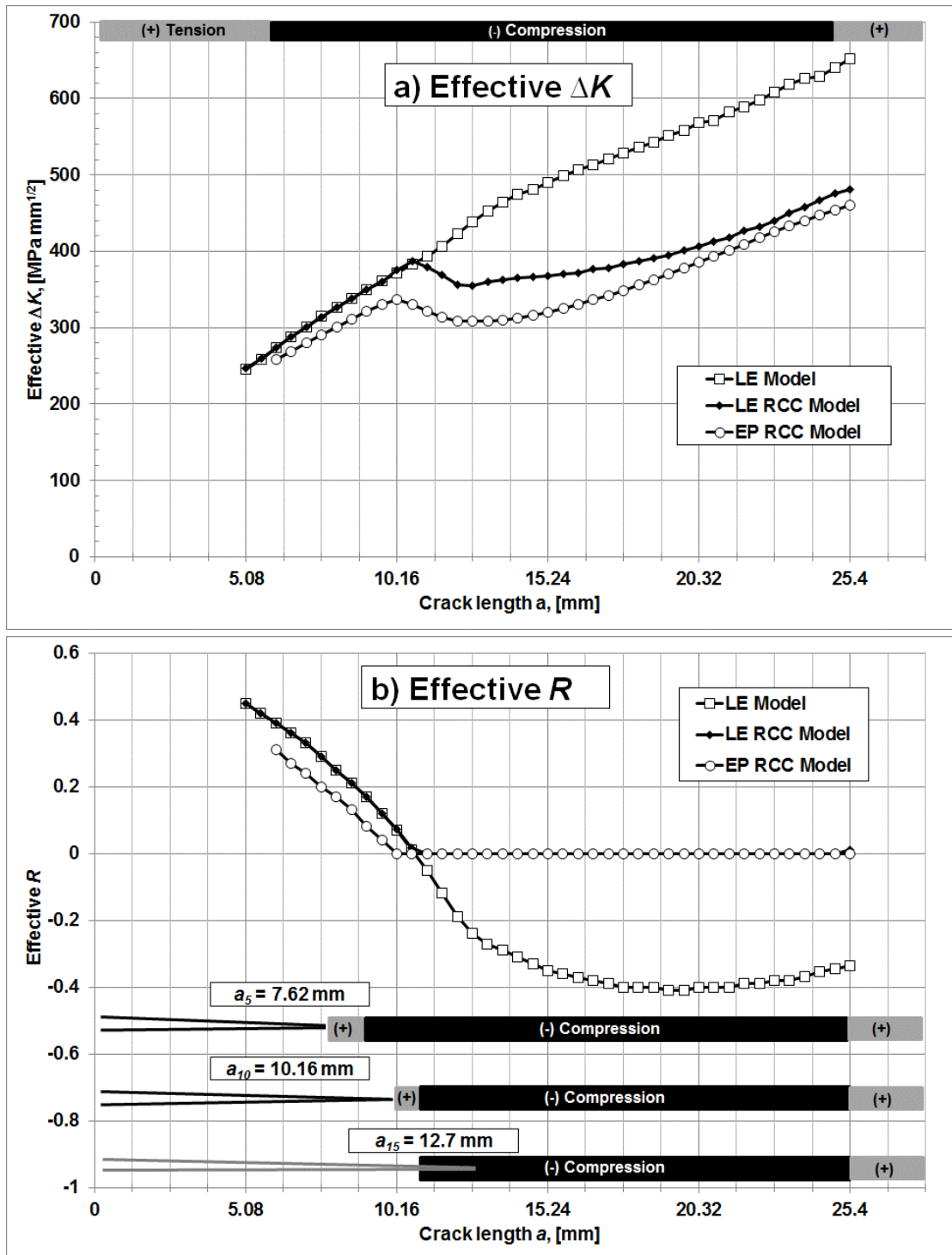


Figure 8. Fatigue crack growth model results for the nominal $R=0.05$: a) The effective stress intensity factor range ΔK , and b) the effective stress ratio R .

The $R(a)$ dependence has a different character in the case wherein the rigid crack closure conditions are used and in the case wherein they are not applied. At the crack length of 10-11

mm both models with the rigid crack closure conditions reach a zero value of the effective R and maintain this value after that. The model without the rigid crack closure conditions produced the $R(a)$ curve reaching negative R values with the minimum at ~ 20 mm. The divergence of the two types of curves produced by the LE model and the LE RCC or EP RCC models occurs at the crack length larger than that corresponding to the change in the original RS field from tensile to compressive.

Fig. 9 illustrates the FCG rates as a function of the crack length obtained experimentally and using three different computational models. Fig. 9 a shows the full range of crack lengths and Fig. 9 b shows the part of the curve for a smaller range of crack lengths corresponding to stage II FCG process. The bar at the top of Fig. 9 a shows the stress state types in the original RS field and the bars at the bottom of Fig. 9 b demonstrate the stress state types in the redistributed RS field for three different crack lengths. $da/dN(a)$ curves obtained both experimentally and using all different computational models demonstrate the increasing rate of the FCG up to crack length of 10-11 mm. After that the FCG rate decreases up to the crack length of 12-13 mm and then FCG accelerates continuously until the failure of the specimen. It is easy to note that transition from the initial acceleration of the FCG to deceleration in all cases occurs when the crack tip is at the location wherein the redistributed RS field changes from tension to compression (10-11 mm) which is significantly different from the location where the same change of the stress state type occurs in the original RS field (5.5 mm). It is important to note that the EP RCC model produces results that are in the closest agreement with the experimental data.

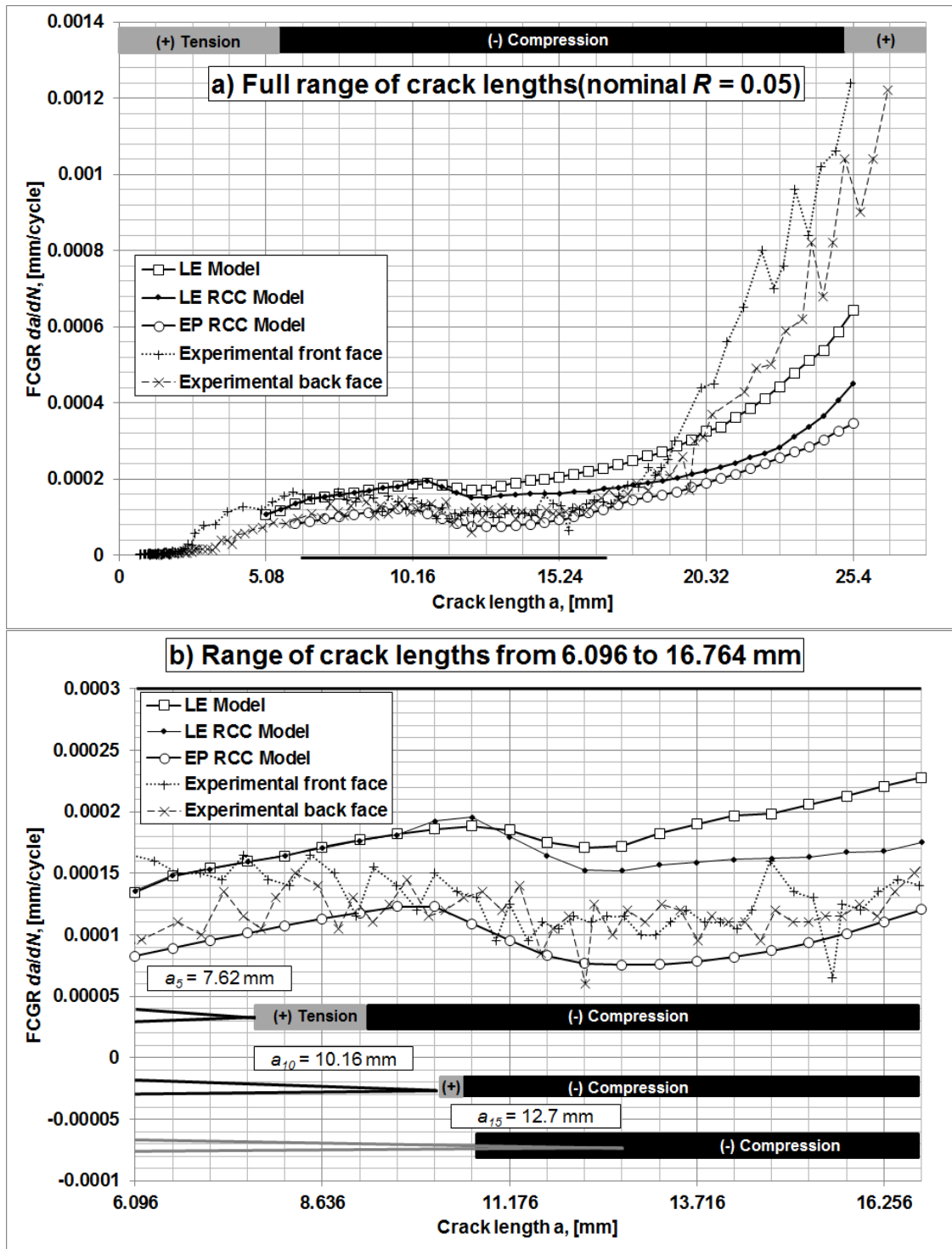


Figure 9. Fatigue crack growth rate as a function of the crack length for a low stress ratio (nominal $R = 0.05$): a) Full range of crack lengths and schematic distribution of the original RSF, and b) crack lengths in the range of $a_6 = 6.096$ mm to $a_{23} = 16.764$ mm, which correspond to stage II of the FCG curve, and schematic distribution of the actual RSF for three crack lengths.

Fig. 10 illustrates the crack length vs. number of cycles curves obtained experimentally and in simulations. For most of the fatigue life the EP RCC model produces a curve closest to the experimental results, though consistently underestimating the crack length. Only at the end of the FCG process when the acceleration of the crack growth at stage III of the FCG occurs does the experimental $a(N)$ curve shift closer to the curve produced by the LE RCC model.

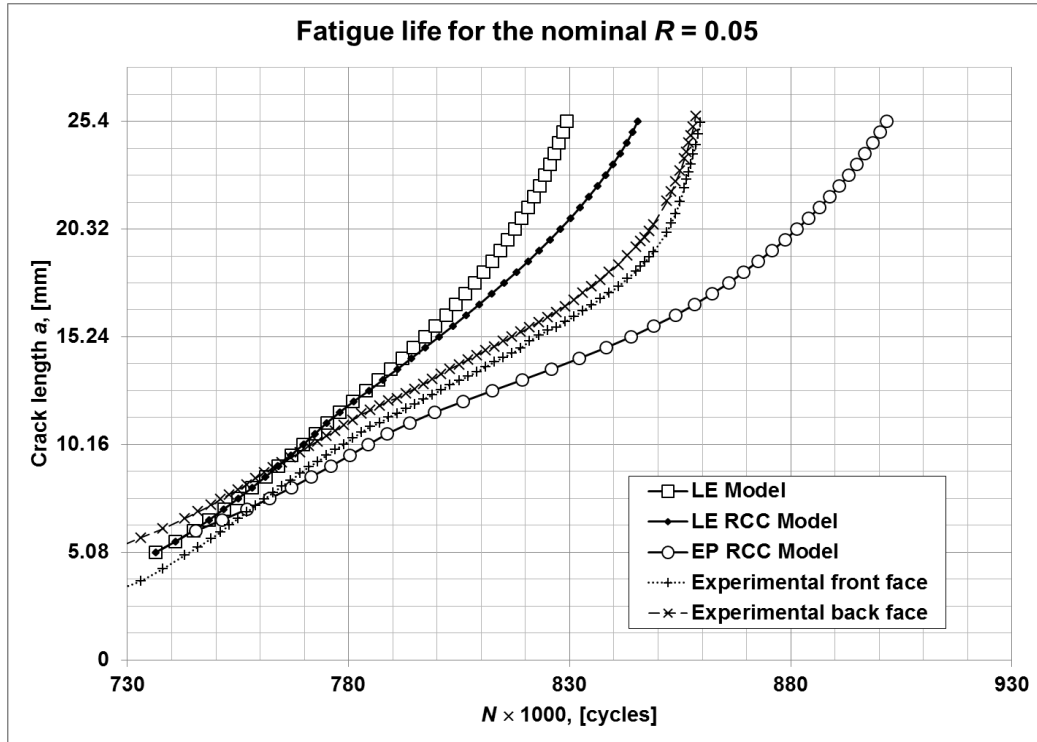


Figure 10. Fatigue life for a low stress ratio (nominal $R = 0.05$) and schematic distribution of the actual RSF.

4.2.2 $R = -1.0$

Fig. 11 a and b present the FCG rates as a function of the crack length in the manner similar to that of Fig. 9 a and b. The FCG accelerates initially as the crack length increases and after reaching the maximum at ~ 7 mm decelerates until the minimum is reached at ~ 13 mm. The transition from the initial acceleration to deceleration occurs under the $R = -1.0$ conditions at a shorter crack length (Fig. 11 b) than under $R = 0.05$ (Fig. 9 b). Also, the deceleration effect is more pronounced at $R = -1.0$ than at $R = 0.05$. The LE model which does not include the rigid crack closure conditions produces the best agreement with the experimental results for the FCG under the $R = -1.0$ conditions.

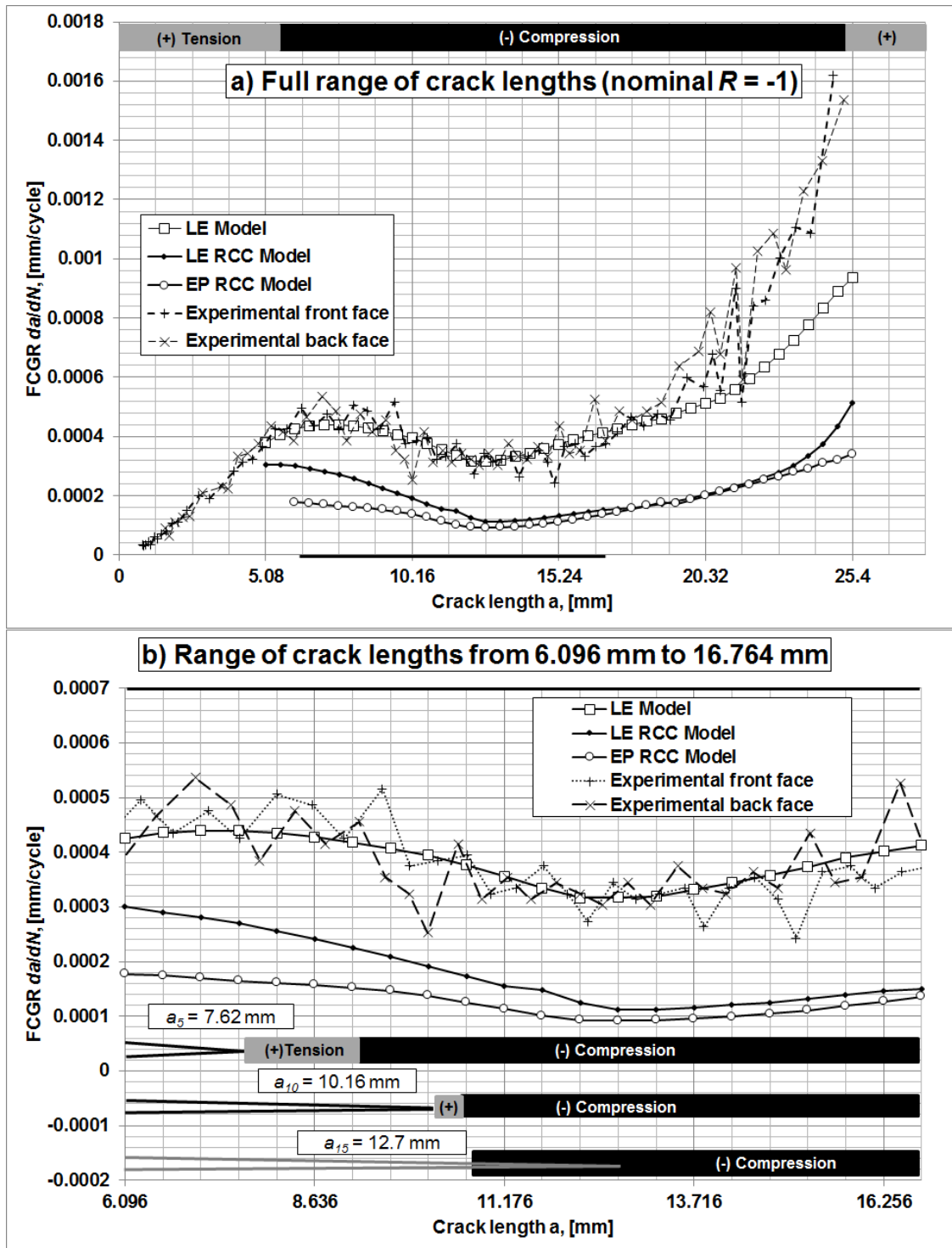


Figure 11. Fatigue crack growth rate as a function of the crack length for a negative stress ratio (nominal $R = -1$): a) Full range of crack lengths and schematic distribution of the original RSF, and b) crack lengths in the range of $a_6 = 6.096$ mm to $a_{23} = 16.764$ mm, which correspond to stage II of the FCG curve, and schematic distribution of the actual RSF for three crack lengths.

Fig. 12 demonstrates the crack length vs. number of cycles curves obtained experimentally and in simulations. For the entire fatigue life, the LE model produces a curve closest to the experimental results with a very good agreement between the experimental data and the simulation results.

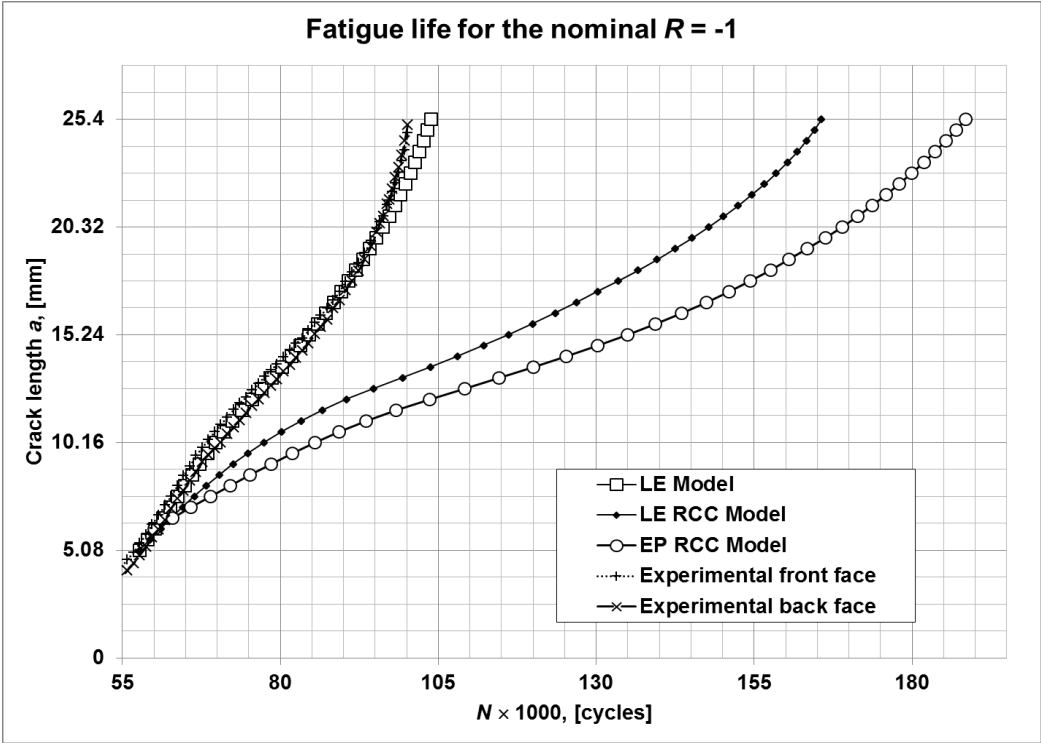


Figure 12. Fatigue life for a negative stress ratio (nominal $R = -1$) and schematic distribution of the actual RSF.

4.3 Discussion

The results of the experimental study and computer simulations demonstrate several important features that should be taken into account when analyzing the FCG in the materials with the RS fields.

Feature One:

The redistribution of residual stresses resulting from the crack propagation can play an important role leading to the development of different modes of crack growth (i.e., with and without crack closure) during the FCG process. For example, in the experiments and models of the FCG under the load cycles with the nominal stress ratio $R = 0.05$, the deceleration of the crack growth rate occurs at the crack length of 10-11 mm (Fig. 9). This length coincides with the length at which the redistributed RS field at the crack tip changes from tensile to compressive, and where the crack closure becomes possible. The original RSF in the un-notched specimen changes from tensile to compressive at the depth of 5.5 mm from the surface of the specimen. Therefore, the change in the growth rate (the retardation) is produced at the crack length determined by the redistributed RSF and not by the original RSF. If the original RSF were used within a simple superposition model, then the crack growth retardation would be starting at the crack length of 5.5 mm. Such a model would underestimate the growth rate and produce less conservative results. It is necessary to note, that if the first RSF region through which the crack propagates is compressive, then the stress redistribution will delay the transition from the compressive to tensile stress and enhance the level of compressive stresses. In such a situation, typical for the effects of a cold-hole expansion or shot peening treatments on the FCG originating from the treated surface, the omission of stress redistribution effects results in the overestimation of the crack growth rate and produces more conservative estimates.

In the case of the FCG test and simulations with the nominal $R = -1.0$, the crack closure occurs at all the crack lengths with the crack tip in both the tensile and compressive RSF regions. In this case, the deceleration of the crack growth starts when the crack tip is still in the tensile redistributed RSF region (Fig. 11), although, as the crack propagates into the compressive region of the redistributed RSF, the growth rate continues to decrease. At the length of ~ 12 mm the effect of the increase in the crack length on the effective K_{max} becomes more important than the reduction in the effective R , and the crack growth starts to accelerate with the increase in K_{max} .

Feature Two:

A comparison of the results of the FCG experiments with the simulation results indicates that under distinctive R -values different types of simulation models produce a better agreement with the experimental data. This difference can be related to the importance of the crack closure

effects and how they are accounted for in the effective ΔK calculation, and to the accuracy of the Harter T-method at different values of R_{int} .

In the tests and simulations with $R = 0.05$, the model with rigid crack closure conditions and with a plastic wake effect results in crack growth rates which are in the best agreement with the experimental results within stage II of the FCG (Fig. 9). It slightly underestimates the growth rate while two other models (with rigid crack closure conditions but without the plastic wake, and without both rigid crack closure conditions and the plastic wake) produce significantly overestimated growth rates. When the crack tip reaches the region of the compressive redistributed RSF, the difference between the crack growth rate in the model with the rigid crack closure conditions and plastic wake effect and that in the experimental results shows a slight increase resulting in a larger underestimation of the crack growth rate of the model. However, this model still remains the closest to the experimental data as compared to other models. This effect can be related to the effective ΔK calculation method using rigid crack closure conditions. In this approach the minimum value of the effective stress intensity, K_{min} , is limited by the zero value, and it is considered that in the FCG the negative part of the stress cycle does not produce any contribution to the driving force for the FCG. Such an approximation is still commonly used in practice [35] and presented in many textbooks; however, it has been shown that it can lead to the underestimation of the FCG rate [9]. The negative part of the load cycle produces some contribution to the FCG driving force and increases the overall FCG rate, though not as significantly as the positive part.

The negative effect of the omission of the contribution from the negative part of the stress cycle from the FCG driving force becomes more pronounced in the case of the simulation of the FCG under the cyclic load with the nominal $R = -1.0$. In this case, the model without both the rigid crack closure conditions and the plastic wake produces the FCG rates closest to the experimentally observed (Fig. 11). The introduction of the rigid crack closure conditions results in a significant underestimation of the FCG rate. When the rigid crack closure conditions are used together with the plastic wake, the difference between the experimental and computational results becomes even worse. These effects are produced because the introduction of the rigid crack closure conditions results in the elimination from the FCG driving force of the part of the cycle with a negative effective stress intensity. The addition of the plastic wake effect shifts the

crack closure towards higher effective K values and, thus, further reduces the FCG driving force in the computational model.

The contribution from the negative part of the load cycle can also be illustrated by the comparison of the FCG obtained in experiments with $R = 0.05$ and $R = -1.0$. The maximum load in these cycles was the same and if the negative part of the load cycle were discarded, then almost the same load range would be produced: 33.25 kN for $R = 0.05$ vs. 35 kN for $R = -1.0$. The stress intensity ranges would be also very close to each other in such a case. However, the FCG rate, in the initial accelerating part of the FCG process, is larger at $R = -1.0$, as compared to that at $R = 0.05$. For instance, at $R = -1.0$ the FCG rate is 0.52 $\mu\text{m}/\text{cycle}$ and at $R = 0.05$ the FCG rate is 0.13 $\mu\text{m}/\text{cycle}$ for the crack length of 7.62 mm. Similarly, the decelerating effect is also much stronger. For instance, at $R = -1.0$ the FCG rate is 0.43 $\mu\text{m}/\text{cycle}$ and at $R = 0.05$ the FCG rate is 0.12 $\mu\text{m}/\text{cycle}$ for the crack length of 11.684 mm. Therefore, for the modeling of the FCG with large negative effective R values (resulting from either the applied load or the RSF) it can be important to develop a FCG model that more accurately represents the negative stress effect on the FCG rate.

In [9] it was suggested that when a full crack closure is achieved, the rigid crack closure condition should be removed. A simple superposition was used in this case in [9]. In the present study, a model with the RSF redistribution and effective K calculation without the rigid crack closure conditions was used. In both [9] and present study a good agreement with the experiment was obtained; however, such an ad-hoc solution does not have any theoretical substantiation and the limits of its applicability are not known. A better understanding of the role of the negative part of the load cycle in the FCG and the knowledge of the physical mechanisms involved in it are necessary for the development of more physics-based FCG models for such conditions.

Conclusions

A well-defined, consistent and repeatable Residual Stress (RS) field was experimentally produced in Al7050-T7451 specimens using a four-point-bending test setup. The RS field was accurately matched by an elastic-plastic FE model that used a yield strength at the 0.025% proof stress and a combined hardening model.

A FCG model based on a novel effective K definition was developed. The model considered the redistributed RSF due to the FCG, in combination with crack closure and plastic

wake effects. The comparison of the experimental data and simulation results demonstrated that the elastic-plastic model with crack closure and plastic wake effects provides the closest prediction of the experimental results for the FCG with positive applied stress ratios. The model accurately reproduced the FCG deceleration in the presence of a compressive zone RS field. However, in the case of a negative stress ratio, all models with crack closure effects strongly underestimated the FCG rates, and the linear elastic model provided a better agreement with the experimental data. The obtained results demonstrate that the negative part of the stress cycle with a fully closed crack contributes to the driving force for the FCG and, thus, should be accounted for in the fatigue life estimates. Furthermore, the onset of the crack closure effect and the deceleration of the crack growth rate for positive applied stress ratios in the FCG tests was determined by the redistribution of the RS fields.

Acknowledgments

C. Garcia gratefully acknowledges the financial support of the Consejo Nacional de Ciencia y Tecnologia (CONACyT, grant 309064) and the Roberto Rocca Education Program (RREP).

A. Artemev gratefully acknowledges the support of NSERC (grant 155157-2010).

References

- [1] P.J. Withers, H.K.D.H. Bhadeshia, Residual stress: I. Measurement techniques, *Mater. Sci. Technol.* 17 (2001) 355-365
- [2] P.J. Withers, H.K.D.H. Bhadeshia, Residual stress: II. Nature and origins, *Mater. Sci. Technol.* 17 (2001) 366-375
- [3] Properties of wrought aluminum and aluminum alloys, in: *Properties and selection: Nonferrous alloys and special-purpose materials*, Vol 2, ASM Handbook, ASM International, 1990, pp 62-122
- [4] ANSI/AWS D1.1 Structural welding code – Steels, American Welding Society, 2010.
- [5] BS 7910 Guide to methods for assessing the acceptability of flaws in metallic structures, British Standard, 2015.
- [6] Handbook for Damage Tolerant Design, U.S. Air Force, published on the internet at <http://www.afgrow.net/applications/DTDHandbook/>. [Accessed May, 2015].

- [7] M. Beghini, L. Bertini, Fatigue crack propagation through residual stress fields with closure phenomena, *Engng. Fract. Mech.* 3 (1990) 379-387
- [8] M. Beghini, L. Bertini, E. Vitale, Fatigue crack growth in residual stress fields: Experimental results and modelling, *Fatig. Fract. Engng. Mater. Struct.* 17 (1994) 1433-1444
- [9] K.W. Jones, M.L. Dunn, Fatigue crack growth through a residual stress field introduced by plastic beam bending, *Fatigue Fract. Eng. Mater. Struct.* 31 (2008) 863-875
- [10] K.W. Jones, M.L. Dunn, Predicting corner crack fatigue propagation from cold worked holes, *Engng. Fract. Mech.* 76 (2009) 2074-2090.
- [11] J.E. LaRue, S.R. Daniewicz, Predicting the effect of residual stress on fatigue crack growth, *Int. J. Fatigue* 29 (2007) 508-515
- [12] W. Elber, Fatigue crack closure under cyclic tension, *Engng Frac. Mech.* 2 (1970) 37-44.
- [13] K. Solanki, S. R. Daniewicz and J. C. Newman Jr., "Finite element analysis of plasticity-induced fatigue crack closure: an overview," *Engng. Fract. Mech*, vol. 71, pp. 149-171, 2004.
- [14] Liu A.F., The effect of residual stresses on crack growth from a hole, NOR 79-74. Northrop Corporation Aircraft Group; 1979.
- [15] A. P. Parker, Residual stress effects in fatigue, *ASTM STP*, vol. 776, pp. 13-31, 1982.
- [16] A. Todoroki and H. Kobayashi, Prediction of fatigue crack growth rate in residual stress fields, *Key Eng Mater*, Vols. 51-52, pp. 367-372, 1991.
- [17] A. T. Ozdemir and L. Edwards, Relaxation of residual stresses at cold-worked fastener holes due to fatigue loading, *Fatig. Fract. Engng. Mater. Struct.*, 20, (1997) 1443-1451.
- [18] M. E. Fitzpatrick and L. Edwards, Fatigue crack/residual stress field interactions and their implications for damage-tolerant design, *J Mater Eng Perfor*, 17(2) (1998) 190-198.
- [19] Y. C. Lam and K. S. Lian, The effect of residual stress and its redistribution on fatigue crack growth, *Theoretical and Applied Fracture Mechanics* 12 (1989) 59-66.
- [20] T. M. Hsu and W. M. McGee, Extended study of flaw growth at fastener holes, Technical report AFFDL-TR-77-83, 1977.
- [21] W. H Cathey and A. F. Grandt-Jr., Fracture mechanics consideration of residual stresses introduced by coldworking fastener holes, *J Eng Mater Tech*, 102(1) (1980) 85-91.
- [22] G. Clark, Modeling residual stresses and fatigue crack growth at cold-expanded fastener holes, *Fatig. Fract. Engng. Mater. Struct.*, 14(5) (1991) 579-589.
- [23] Z. Wang and X. Zhang, Predicting fatigue crack growth life for cold-worked holes based on existing closed-form residual stress models, *Int. J. Fatigue*, 25 (2003) 1285-1291

- [24] M. Kokaly, J. Ransom, B. Jude, H. Restis and L. Reid, Observations and analysis of fatigue crack growth from cold worked hole, Proceedings of the 8th Joint FAA/DoD/NASA aging aircraft conference, Palm Springs, CA, 2005.
- [25] Z.T. Tang, Z.Q. Liu, Y.Z. Pan, Y. Wan, X. Ai, The influence of tool flank wear on residual stresses induced by milling aluminum alloy, *J. Mater. Process. Technol.* 209 (2009) 4502-4508.
- [26] ASTM-E647, Standard Test Method for Measurement of Fatigue Crack Growth Rates, American Society for Testing and Materials, 2011.
- [27] J. Ahmad, V. Papaspyropoulos, A. T. Hopper, Elastic-plastic analysis of edge-notched panels subjected to fixed grip loading, *Engng. Fract. Mech.* 38 (1991) 283-294.
- [28] H. X. B. Pan, K. Qian, A. Asundi, Two-dimensional digital image correlation for in-plane displacement and strain measurement: a review, *Meas. Sci. Technol.* 20 (2009) 062001 (17pp)
- [29] M.B. Prime, Residual stress measurement by successive extension of a slot: The crack compliance method, *Appl. Mech. Rev.* 52(2) (1999) 75-96
- [30] J.A. Harter, in: Afgrow users guide and technical manual, AFRL-VA-WP-TR-1999-3016; 1999
- [31] ABAQUS Version 6.11-2, Simulia Corp., Providence, RI, 2011
- [32] D.R.J. Owen, A.J. Fawkes, Engineering fracture mechanics: numerical methods and applications, Pineridge Press Ltd., Swansea U.K. 1983
- [33] V.D. Lacarac, A.A. Garcia-Granada, D.J. Smith, M.J. Pavier, Prediction of the growth rate for fatigue cracks emanating from cold expanded holes, *Int. J. Fract.*, 26, (2004) 585-595.
- [34] W. Cheng, I. Finnie, An overview of the crack compliance method for residual stress measurement, Proceedings of the Fourth International Conference on Residual Stresses, Baltimore, MD 449-558
- [35] G. Totten, Fatigue crack propagation, *Advanced Materials & Processes*, Vol. 166, pp. 39-41, 2008.